INORGANIC CHEMISTRY FRONTIERS

RESEARCH ARTICLE

View Article Online
View Journal | View Issue

Cite this: *Inorg. Chem. Front.*, 2023, **10**, 4414

In situ growth of MOF-derived nitrogen-doped carbon nanotubes on hollow MXene spheres for K-ion storage†

Xiaoyu Chen, Shuanghong Xia, Tianyu Tan, Yajing Zhu, Ling Li, * Qiancheng Zhu* and Wenming Zhang *

Received 27th April 2023,
Accepted 18th June 2023

DOI: 10.1039/d3qi00763d

rsc.li/frontiers-inorganic

Two-dimensional (2D) MXenes have the potential as electrode materials for energy storage owing to their unique structural properties and excellent electrochemical properties. Unfortunately, MXene nanosheets easily stack due to van der Waals forces, which degrade the electrochemical performance of MXene-based materials. Herein, the three-dimensional (3D) structure of hollow spheres constructed by 2D MXene nanosheets using a template method can effectively reduce the stacking of MXene nanosheets. However, electron conduction is hampered by the gaps between the MXene spheres. To enhance the conductivity between MXene spheres, sea urchin-like hollow MXene spheres coupled with metal organic frame (MOF)-derived nitrogen-doped carbon nanotubes (CoN-CNT@SMXene) were synthesized by *in situ* tip growth of nitrogen-doped carbon nanotubes with CoN-capped tips on the surface of MXene hollow spheres. The cross-linked nanotubes drastically enhanced the connections of the MXene hollow spheres and provided a superior electron and ion migration bridge. When applied as an anode in potassium-ion batteries (PIBs), CoN-CNT@SMXene performs much better than the bare MXene spheres in terms of capacity, current rate and cycle stability. The capacity still maintained 253 mA h g^{-1} at 400 mA g^{-1} for 1000 cycles. This study inspires the development of high-performance MXene-based materials in K-ion batteries.

1 Introduction

Nowadays, high-performing, low-cost new-generation batteries are the most promising choices for portable electronic devices and electric vehicles.[1–5] Potassium-ion batteries (PIBs) are a high potential candidate owing to their fast ion conduction and high working voltage.[6–10] However, the large radius of K^+ (1.38 Å) causes significant volume changes during charge/discharge, resulting in structural instability of the electrode.[11–13] To meet commercial standards and facilitate the diffusion of K^+ ions, further development of anode materials with enhanced electrochemical performance is urgently needed.[14] Two-dimensional (2D) materials have become attractive in the field of energy storage because of their particular structural properties and excellent electrochemical properties.[14–16] Currently, 2D materials, such as graphene,[17,18] boron nitride,[19] transition metal dihalides (TMDs),[20,21] black phosphorus,[22] transition metal carbides/nitride (MXene),[23,24] and silicene,[25] have been extensively investigated in chemistry, materials science, and nanotechnology.[25–27] Among them, MXene is a graphene-like two-dimensional-layered material composed of $M_{n+1}X_nT_x$ elements (M represents transition metal elements, X represents C or N, and T represents functional groups).[28,29] MXene has been greatly studied as an anode for PIBs owing to its high mobility, abundant surface functional groups and strong flexibility.[30–36] Among the many members of MXenes, $Ti_3C_2T_x$ is the most focused configuration, especially in energy storage materials. Owing to its excellent electrical conductivity, abundant electrochemically active sites and excellent mechanical flexibility, $Ti_3C_2T_x$ is considered one of the most potential electrode materials.[37,38]

However, MXene nanosheets are interlinked by van der Waals forces and hydrogen bonds, leading to the stacking and agglomeration of sheets, which limits the transfer of charged ions between layers and thus hinders the kinetics of redox reactions.[39] A series of stacking prevention strategies are proposed to fully use MXene nanosheets for energy storage. One strategy is to introduce embedding layers (*e.g.*, carbon nanoparticles, polymers, metal oxide nanoparticles, and large ions) to optimize energy storage performance.[40–43] Unfortunately, these materials exhibit suboptimal structural stability and few active sites, which results in rapid capacity decay and slow redox reactions during cycling. Another common strategy is to

Province-Ministry Co-construction Collaborative Innovation Center of Hebei Photovoltaic Technology, College of Physics Science and Technology, Hebei University, Baoding, Hebei 071002, China. E-mail: lilinghbu@163.com, whqianchengzhu@163.com, wmzhanghbu@126.com

† Electronic supplementary information (ESI) available. See DOI: https://doi.org/10.1039/d3qi00763d

design a 3D structure that can effectively improve ion and electron transport rates in electrode materials. For instance, Zhao *et al.* reported a 3D porous MXene foam fabricated with a sulfur template directly as the electrode, which is flexible, self-supporting, and fast electron transfer.[44] The unique 3D porous structure exposed massive reaction sites to improve electrochemical performance. Furthermore, Xia *et al.* designed a vertically aligned $Ti_3C_2T_x$ electrode fabricated using the mechanical shearing of layered $Ti_3C_2T_x$ sheets.[45] The electrode benefits from its vertically arranged structure, which reduces ion transport resistance and provides numerous active sites. Hence, 3D constructs of MXene nanosheets have been regarded as one of the most efficient methods, avoiding the problem of nanosheet stacking and exposing many active sites.

Herein, we report the processing of MOF-derived nitrogen-doped carbon nanotubes on hollow MXene spheres (CoN-CNT@SMXene) *via* sacrificial poly (methyl methacrylate) (PMMA) spherical templates, followed by *in situ* tip growth of nitrogen-doped carbon nanotubes derived from MOF. Owing to the fabrication of carbon nanotubes catalyzed by Co monomer, single hollow MXene spheres are linked by nitrogen-doped carbon nanotubes. Cross-linked carbon nanotubes provide superior electron and ion transport bridges, improving the conductivity of these MXene spheres. Simultaneously, the 3D porous structure offers massive active sites and ion migration channels for the redox reaction, which improves the electrochemical performance of the PIBs. Benefiting from the above fascinating merits, the CoN-CNT@SMXene electrode with superior electrochemical properties delivered a high reversible capacity (306 mA h g^{-1} at 100 mA g^{-1}), inspiring rate capability (231 mA h g^{-1} at 3.2 A g^{-1}), and excellent cycling performance (253 mA h g^{-1} at 400 mA g^{-1} for 1000 cycles).

2 Experimental section

2.1 Preparation of $Ti_3C_2T_x$ colloidal solution

The $Ti_3C_2T_x$ nanosheets were obtained by etching. 1.0 g Ti_3AlC_2 powder (11 Technology Co., Ltd) was etched with 10 mL of hydrofluoric acid (HF) aqueous solution and stirred at 35 °C for 24 hours. Then, the above product was washed by centrifugation with deionized water until the supernatant pH reached above 6. Subsequently, the above precipitate was layered in 10 mL of 25 wt% tetrapropylammonium hydroxide (TPAOH) aqueous solution with shaking under an ice bath for 6 h. Finally, the $Ti_3C_2T_x$ colloidal solution was obtained.

2.2 Fabrication of $Ti_3C_2T_x$/PMMA hybrid spheres

First, 2 mL PMMA spherical dispersion (10 mg $mL^{-1)}$ is thoroughly mixed with 1 mL $Ti_3C_2T_x$ colloidal solution (2 mg mL^{-1}) for 10 minutes, followed by centrifugation to collect the solid powder. The powder was centrifuged with deionized water at 3500 rpm for 10 minutes. Then, the above precipitates were dried under a vacuum at 60 °C overnight. These $Ti_3C_2T_x$/PMMA hybrid spheres were calcined (annealed at 450 °C for 1 h under an argon atmosphere) to remove PMMA, and SMXene samples were obtained.

2.3 Manufacturing of CoN-CNT@SMXene

Typically, the as-obtained $Ti_3C_2T_x$/PMMA hybrid sphere solution (20 mL, 5 mg mL^{-1}) and polyvinyl alcohol pyrrolidone (PVP) solution (20 mL, 10 mg mL^{-1}) are well mixed. Then, 20 mL of $Co(NO_3)_2{\cdot}6H_2O$ (1 mmol) solution and 20 mL of 2-methylimidazole (8 mmol) solution were sequentially added to the above-mixed solution and stirred well. The ZIF-67@$Ti_3C_2T_x$/PMMA hybrid spheres were collected by centrifugation and freeze-drying methods.

These ZIF-67@$Ti_3C_2T_x$/PMMA hybrid spheres were calcined (annealed at 450 °C for 1 h under an argon atmosphere) to remove PMMA, and ZIF-67@$Ti_3C_2T_x$ samples were obtained. The prepared ZIF-67@$Ti_3C_2T_x$ is then mixed with melamine in proportion to a ceramic crucible. The above product was annealed at 800 °C under an H_2/Ar atmosphere for 2 h to obtain CoN-CNT@SMXene samples. Under the same conditions, Co@SMXene samples were obtained without melamine.

2.4 Material characterizations

Scanning electron microscopy (SEM, JEOL S-4800) and transmission electron microscopy (TEM, JEOL-2100) were used to characterize the morphology and microstructure of the samples. The crystal structure was tested with X-ray diffraction (XRD) (Cu Kα radiation, Bruker AXS D8, λ = 1.5418 Å) in the range of 10–80° (2θ), where the step scan was 0.02° and the residence time was 0.5 s. The chemical state of the sample was tested using X-ray photoelectron spectroscopy (XPS) (ESCALAB Type 250XI, Al-Kα radiation (8.34 Å)). A specific surface area analyzer (NOVA2200 Analyzer) was used to determine the specific surface area and pore size distribution of the samples.

2.5 Electrochemical measurements

Electrochemical measurements were performed with CR2032 coin-type cells in which K foil, glass fiber, and 0.8 M KPF_6 dissolved in ethylene carbonate (EC) and diethyl carbonate (DEC) (1/1 Vol%) served as counter electrodes, separators, and electrolytes, respectively. The working electrodes comprise as-prepared powder, acetylene black and polyvinylidene fluoride mixed in *N*-methylpyrrolidone at a ratio of 7 : 2 : 1. The galvanostatic charge–discharge (GCD), rate, cycling performance and galvanostatic intermittent titration technique (GITT) tests were conducted on the battery test system (LAND CT2001A) with the voltage ranging from 0.01 to 3.0 V *versus* K^+/K. Cyclic voltammetry (CV) tests at different scan rates were conducted using a VMP_3 potentiostat (Biologic, France) in the voltage range of 0.01–3.0 V (*vs.* K^+/K). Electrochemical impedance spectroscopy (EIS) was tested in the frequency range of 10 mHz–100 kHz.

2.6 Computational details

All density functional theory (DFT) calculations were employed by the Vienna Ab Initio Computation Package (VASP) in

Generalized Gradient Approximation (GGA), which used Perdew, Burke, and Enzerhof (PBE) formulas.[46–48] Projected augmented wave (PAW) potentials were used to describe the ionic cores. A plane wave basis set with a kinetic energy cutoff of 520 eV is used to describe valence electrons.[49,50] Dispersion interactions were described by applying Grimme's DFT-D3 method.[51] The 5 × 5 × 5 Monkhorst–Pack *k*-point grid was used to optimize the Brillouin zone sampling equilibrium lattice constant of CN cells. Moreover, the 4 × 4 × 1 Monkhorst–Pack format *k*-point grids were used to investigate the state density of the structures. The vacuum spacing perpendicular to the plane of the structure is 18 Å. The surface structure sampled by 2 × 2 × 1 Monhorst Package *k*-point sampling was used for the Brillouin zone integral. The migration barrier of K ions in the structures was calculated by the Climbing Image-Nudged Elastic Band methods.

3 Results and discussion

Fig. 1a depicts the fabrication process of the CoN-CNT@SMXene. First, the MXene nanosheets naturally wrap the surface of the PMMA spheres, which is driven by the surface functional groups of the MXene nanosheets. Then, ZIF-67@MXene/PMMA spheres were obtained by a one-pot synthesis, in which Co^{2+} was adsorbed on the MXene surface through a robust electrostatic interaction between Co^{2+} and the electronegative functional group. Finally, CoN-CNT@SMXene spheres were obtained after a calcination process, and carbon nanotubes were grown on the MXene surface under the catalysis of cobalt. Fig. 1b illustrates the schematic diagram of electron transmission for pure MXene spheres and the CoN-CNT@SMXene spheres. For pure Mxene spheres, although electrons can easily transfer to their spheres, the natural gaps between the MXene spheres result in poor conductivity. In contrast, the nitrogen-doped CNT network in CoN-CNT@SMXene has strong electrical conductivity, which not only promotes the migration of electrons and ions between MXene spheres but also increases the number of active sites.

The scanning electron microscopy (SEM) image in Fig. 2a shows the morphologies of the PMMA spheres. The PMMA spheres with a diameter range of 1–2 μm have smooth surfaces. Fig. 2b shows the $Ti_3C_2T_x$/PMMA hybrid spheres, and the rough surface of the spheres reveals that the $Ti_3C_2T_x$ sheets were successfully wrapped on the surface of the PMMA precursors. In addition, Fig. S1† shows the morphologies of SMXene, part of which are preserved after the removal of the PMMA template. The instability of the structure affects its electrochemical performance. In contrast, the skeleton of the MXene spheres of the CoN-CNT@SMXene composite is well preserved (Fig. 2c). In addition, the surface of MXene has successfully grown carbon nanotubes with spherical particles wrapped in the tips. The microspheres were connected by CoN-CNT, forming a good conductive channel. As shown in Fig. 2d, the transmission electron microscope (TEM) image further confirms the morphology of the CoN-CNT@SMXene. The diameter of the MXene inner shell is about 1.7 μm, which is similar to the size of the PMMA spheres. The growth of carbon nanotubes tightly connected the MXene spheres. Fig. 2(e and f) shows the carbon nanotubes with a diameter of about 29.4 nm extending from the surface of $Ti_3C_2T_x$, and the tips contain spherical nanoparticles with a diameter of about 38.4 nm. The nanotubes were exposed to a typical (002) plane with lattice fringes spaced at about 0.34 nm (Fig. 2g). Moreover, the

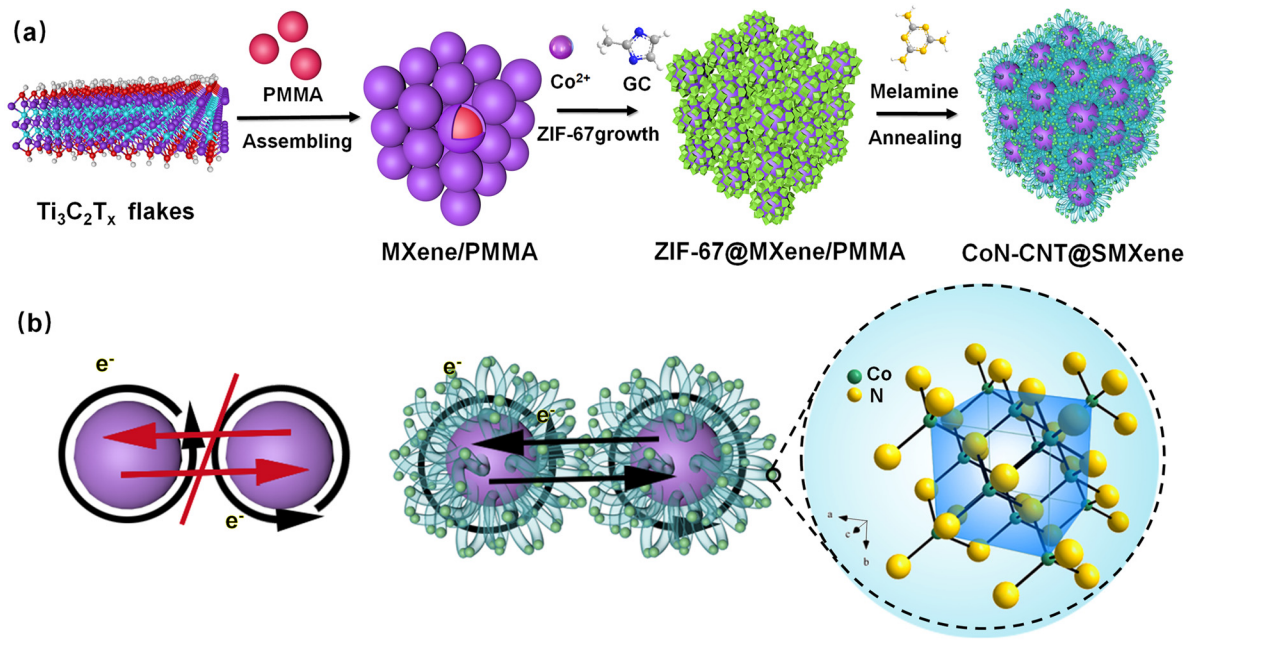

Fig. 1 (a) Schematic illustration of the synthesis process of CoN-CNT@SMXene. (b) Schematic illustrating electron transfer in CoN-CNT@SMXene.

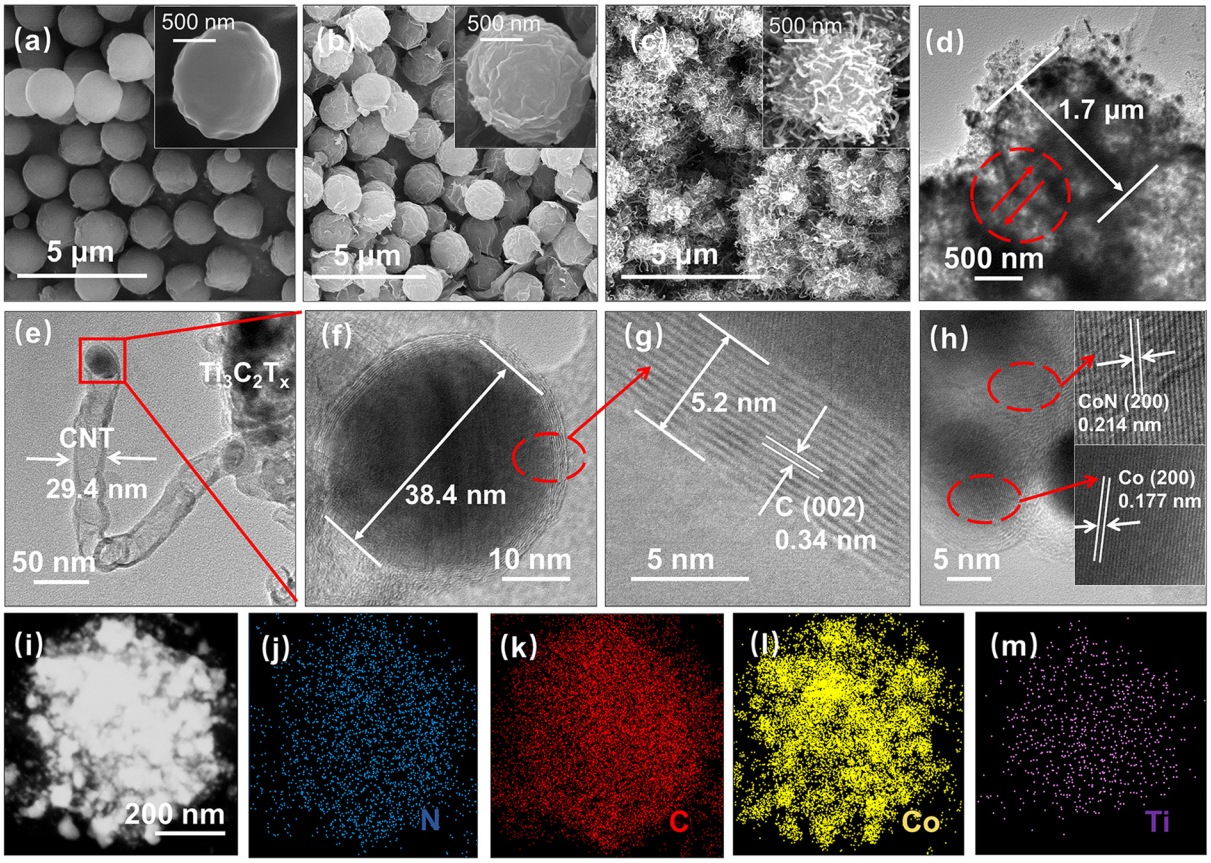

Fig. 2 Scanning electron microscopy (SEM) images of PMMA (a), $Ti_3C_2T_x$/PMMA (b), and CoN-CNT@SMXene (c). (d and e) Transmission electron microscope (TEM) image of CoN-CNT@SMXene. (f–h) High-resolution TEM (HRTEM) images of CoN-CNT@SMXene. (i–m) Energy dispersive X-ray spectra (EDS) images of CoN-CNT@SMXene.

HRTEM image of the particle growing on top of the nanotube (Fig. 2h) possesses lattice fringe spacings of 0.177 nm and 0.214 nm, corresponding to the (200) planes of metallic Co and CoN, respectively. The conversion of melamine to CNTs is due to the catalyst of the CoN nanoparticles. Furthermore, energy dispersive X-ray spectra (EDS) of the CoN-CNT@SMXene (Fig. 2i–m) demonstrate that C, N, and Ti are uniformly dispersed on the spheres; notably, Co particles were wrapped at the top of the nanotube. To obtain the content of various elements in CoN-CNT@SMXene, detailed measurements were conducted using ICP-MS and EA methods, as shown in Table S1.† In short, the synthesis of CoN-CNT@SMXene was successful.

The phase identification of Ti_3AlT_x, $Ti_3C_2T_x$, PMMA@$Ti_3C_2T_x$ Co@SMXene and CoN-CNT@SMXene composites is performed *via* XRD patterns (Fig. 3a and S2†). Notably, $Ti_3C_2T_x$ was successfully etched by comparing the diffraction peaks of Ti_3AlT_x and $Ti_3C_2T_x$ (Fig. S2†). In addition, Fig. S2† shows that the diffraction peak of PMMA@$Ti_3C_2T_x$ is different from that of $Ti_3C_2T_x$, which is attributed to the effect of the polymer PMMA on the XRD results. The diffraction peaks of Co@SMXene agree well with the (111), (200) and (220) crystal planes of JCPDS card no.15-0806 for face-centered cobalt crystal. The results indicate that Co particles are formed by the reaction between Co^{2+} ions and carbon.[44] Moreover, several diffraction peaks of CoN-CNT@SMXene located at 41.8°, 47.5° and 62.1° correspond to the (100), (101) and (102) planes of CoN (JCPDS no.16-0116), respectively. It is noteworthy that the graphitic carbon (002) peaks appear at 26° after the calcination process (JCPDS no. 41-1487), suggesting the presence of carbon nanotubes. It is noteworthy that the (002) peak of graphitic carbon at 26° appeared after calcination (JCPDS no. 41-1487), suggesting the presence of CNTs.

The XPS survey spectrum of CoN-CNT@SMXene further verifies the EDS results (Fig. S3†). The N 1s spectrum (Fig. 3b) is resolved into three peaks at 398.6 (pyridinic N), 400.7 (pyrrolic N), and 401.5 eV (graphitic N), revealing that carbon nanotubes were incorporated with N atoms.[52] Theoretically, graphite N is beneficial for reducing conduction losses, while pyridine N and pyrrole N are beneficial for reducing dipole relaxation losses. The high-resolution Co $2p_{3/2}$ spectrum of CoN-CNT@SMXene displays four split peaks at 778.4, 780.5, 783.4 and 786.5 eV, corresponding to Co, Co^{2+}, Co–N and Co–OH, respectively (Fig. 3c), further indicating the successful preparation of CoN.[53] In addition, the presence of Co–OH bonds suggests that oxidation has occurred on the

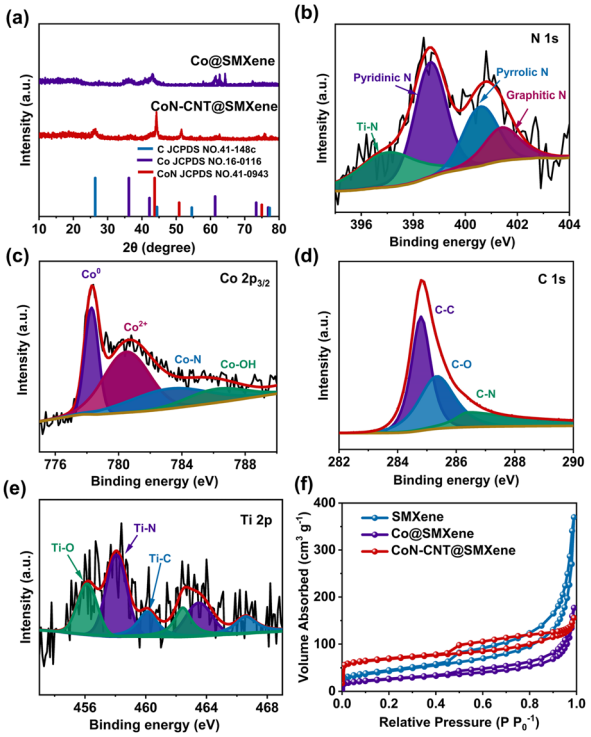

Fig. 3 (a) XRD patterns of Co@SMXene and CoN-CNT@SMXene. (b–e) High-resolution N 1s (b), Co 2p (c), C 1s (d) and Ti 2p (e) XPS spectra of CoN-CNT@SMXene. (f) N_2 adsorption/desorption isotherms.

CoN-CNT@SMXene surface. The C 1s peaks are deconvoluted into three sub peaks (Fig. 3d) near 284.8 (C–C), 285.3 (C–O) and 286.5 eV (C–N), which is consistent with previous reports.[54] The appearance of C–N bonds is due to the pyrolysis reaction of melamine. Moreover, the Ti 2p spectrum is deconvoluted to Ti–O (456.1 and 462.4 eV), Ti–N (458.1 and 463.5 eV), and Ti–C (460.1 and 466.6 eV), indicating that the Ti_3C_2 nanosheet is doped with N atoms (Fig. 3e).[55,56]

Subsequently, the specific surface area and pore size distribution of the SMXene, Co@SMXene and CoN-CNT@SMXene nanostructures were evaluated by N_2 adsorption/desorption measurements. Fig. 3f shows the presence of mesoporous structures in all samples. CoN-CNT@SMXene shows a specific surface area of 253 $m^2\ g^{-1}$, which is better than that of SMXene (153.4 $m^2\ g^{-1}$) and Co@SMXene (91.6 $m^2\ g^{-1}$), as shown in Table S2.† Good electrode/electrolyte contacts benefit from the high specific surface area of the sample during the electrochemical process. Based on the pore size distribution, CoN-CNT@SMXene has abundant pores at the pore size range of 0–1.5 nm, which is related to the CNTs (Fig. S4†). Moreover, these samples have rich mesoporous structures at a pore size of about 3–15 nm, which is related to the spherical MXene. These favorable microstructural characteristics are beneficial for the transfer and penetration kinetics of K^+ ions and other electrolyte components.

The electrochemical performance of CoN-CNT@SMXene was characterized by assembling CR2032-type cells. Cyclical voltammetry (CV) curves of CoN-CNT@SMXene (Fig. 4a) show one pair of reduction/oxidation peaks located at 0.361/0.491 V, which are attributed to the K^+ intercalation/deintercalation process. The above process is expressed as $nK^+ + Ti_3C_2/CN + ne^- \rightleftharpoons K_nTi_3C_2/CN$, which agrees with previous reports.[57–59] The wide peaks of CV curves indicate the pseudocapacitance mechanism of K ions on the surface of MXene nanosheets.[33] An irreversible reduction peak is observed at 0.707 V in the first cathodic scan mainly due to the formation of a stable solid electrolyte interface phase (SEI) film and the irreversible reaction between the surface functional groups (–F, OH, O) of MXene nanosheets and K ions. The galvanostatic charge–discharge (GCD) profiles at different current rates for the CoN-CNT@SMXene electrode are shown in Fig. 4b. At 100 mA g^{-1}, the plateaus voltage of the charge–discharge curve corresponds to the redox peaks on the CV curve. In addition, the CoN-CNT@SMXene electrode has the highest discharge capacity by comparing the GCD profiles of different electrodes (Fig. 4b, S5 and S6†).

Fig. 4c shows the rate capability of the SMXene, Co@SMXene, and CoN-CNT@SMXene electrodes. The reversible capacity of the CoN-CNT@SMXene electrode is 373.6 mA h g^{-1} at the current density of 100 mA g^{-1}, while that of the SMXene and Co@SMXene electrodes were 155.9 and 249.1 mA h g^{-1}, respectively. Even at a high current rate of 3.2 A g^{-1}, the SMXene, Co@SMXene, and CoN-CNT@SMXene electrodes achieved capacities of 70, 104 and 231 mA h g^{-1}, respectively. Relatively speaking, the rate performance of the

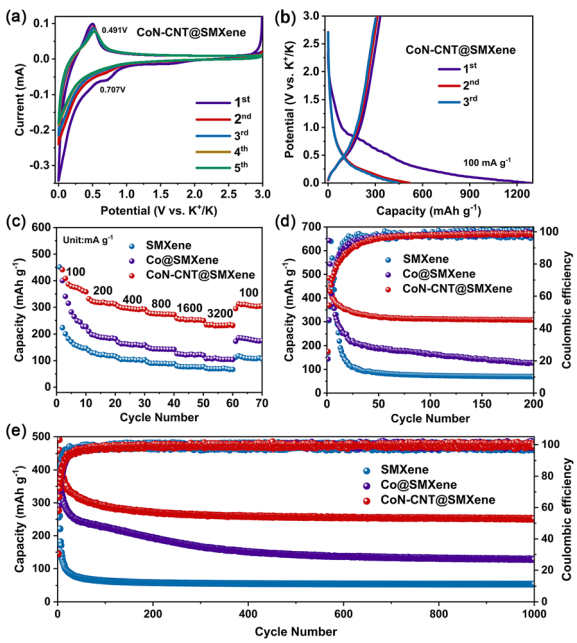

Fig. 4 (a) CVs of CoN-CNT@SMXene at a scan rate of 0.1 mV s^{-1}. (b) Discharge–charge profiles of CoN-CNT@SMXene at 0.1 A g^{-1} at different cycles. (c) Rate capability of SMXene, Co@SMXene, and CoN-CNT@SMXene electrodes. Cycling performance of SMXene, Co@SMXene, and CoN-CNT@SMXene electrodes at (d) 0.1 A g^{-1} for 200 cycles. (e) 0.4 A g^{-1} for 1000 cycles.

CoN-CNT@SMXene electrode exceeds that of most reported MXene-based electrodes (Fig. 4c, S7 and Table S3†) and is even superior to recently reported potassium ion battery anode materials (Table S4†). It was noticed that the CoN-CNT@SMXene exhibited the best rate performance, which is attributed to its rapid ion transfer capability.

Moreover, the CoN-CNT@SMXene electrode exhibits excellent cycling performance with a capacity of 306 mA h g^{-1} at 100 mA g^{-1} and a capacity retention rate of 96% (Fig. 4d), which is better than those of SMXene (70 mA h g^{-1}, 75%), and Co@SMXene (128 mA h g^{-1}, 66%) electrodes. It is noteworthy that the capacity of the CoN-CNT electrode at 100 mA g^{-1} is 131 mA h g^{-1}, which is significantly lower than that of the CoN-CNT@SMXene electrode, indicating that the electrochemical performance contribution of CoN-CNT is small, and its main role is to provide a good electron and ion migration bridge for the MXene hollow sphere (Fig. S8†). Although the capacity of Co@SMXene is high in the first few cycles, the sharp decline in capacity after 10 cycles suggests that CNTs played a key role in strengthening structural interconnections. Even after 1000 cycles, the CoN-CNT@SMXene electrode can achieve a reversible capacity of 252 mA h g^{-1} and a capacity retention rate of 85%, which are superior to those of the SMXene (54 mA h g^{-1}, 71%) and Co@SMXene (128 mA h g^{-1}, 55%) electrodes (Fig. 4e). The cycling performance of the CoN-CNT@SMXene electrode is stable except for the first 50 cycles owing to the activation of the electrode. The CoN-CNT@SMXene electrode exhibits the best stability possibly because the cross-linked nanotubes greatly enhance the connection of the MXene hollow spheres and provide superior electron and ion transport bridges. The detailed mechanism is explored below.

To further elucidate the storage electrochemical kinetics of the CoN-CNT@SMXene anode, CV profiles were conducted at different scan rates from 0.1 to 0.9 mV s^{-1}, as shown in Fig. 5a. The enclosed area of the CV curve represents the total

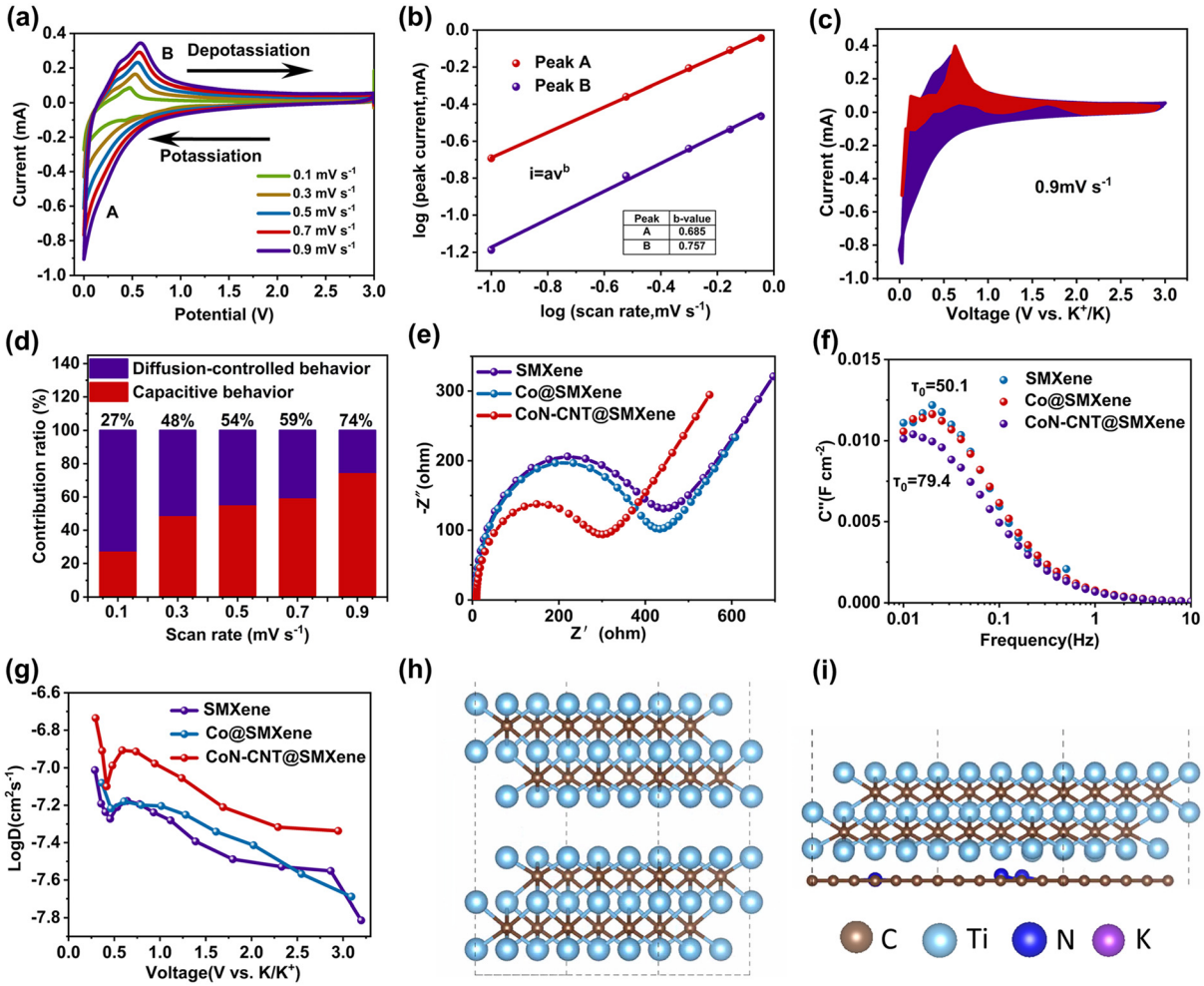

Fig. 5 (a) CV curves of CoN-CNT@SMXene electrode at different scan rates. (b) Log (peak current) *versus* log (scan rate) plot. (c) CV curves separated between the surface capacitive (red region) and total capacitance (purple region) at a scan rate of 0.9 mV s^{-1}. (d) Contribution ratio of capacitive at different scan rates. (e) EIS curves of SMXene, Co@SMXene, and CoN-CNT@SMXene electrodes. (f) Plot of the imaginary part (τ_0) of specific capacitance *vs.* frequency for SMXene, Co@SMXene, and CoN-CNT@SMXene electrodes. (g) K^+ diffusion coefficients. (h) Polyhedral model of Ti_3C_2. (i) nitrogen-doped carbon and MXene layer models.

capacity, comprising diffusion contribution and capacitance contribution and can be expressed as follows:[29]

$$i = av^b, \quad (1)$$

where a and b are variable values. Generally speaking, when b = 1.0, the reaction is mainly a surface control process. However, when b = 0.5, the reaction is mainly controlled by the diffusion process. Fig. 5b displays the logarithmic linear relationship between i and v. The slopes b of the redox peaks are 0.685 and 0.757, revealing the pseudocapacitive behavior of K ions during successive insertion/extraction. The contribution of capacitance is described by the following formula:[60]

$$i = k_1 v + k_1 v^{1/2}, \quad (2)$$

where the first item represents the pseudo-capacitance contribution and the second item represents the diffusion control contribution.[61] The pseudocapacitive contributions are 27, 48, 54, 59, and 74% at different scan rates (Fig. 5c and d), indicating that the pseudocapacitive contribution is dominated at high scan rates, which further demonstrates the ultrafast workability of the CoN-CNT@SMXene electrode.

The electrochemical impedance spectroscopy (EIS) results of SMXene, Co@SMXene, and CoN-CNT@SMXene are shown in Fig. 5e. As expected, the CoN-CNT@SMXene anode shows a lower charge transfer resistance (R_{ct}) of 292.1 Ω than those of SMXene (444.3 Ω) and Co@SMXene (414.1 Ω), demonstrating that CoN-CNT@SMXene provides the fastest electron transport and the highest conductivity. The diffusion capacity of potassium ions can also be further characterized by a relaxation time constant, as shown in Fig. 5f. It is calculated that the relaxation time (τ_0) of CoN-CNT@SMXene is only 12.6 s, which is much shorter than that of SMXene (58.4 s) and Co@SMXene (50.1 s), indicating that CoN-CNT@SMXene has a fast charge

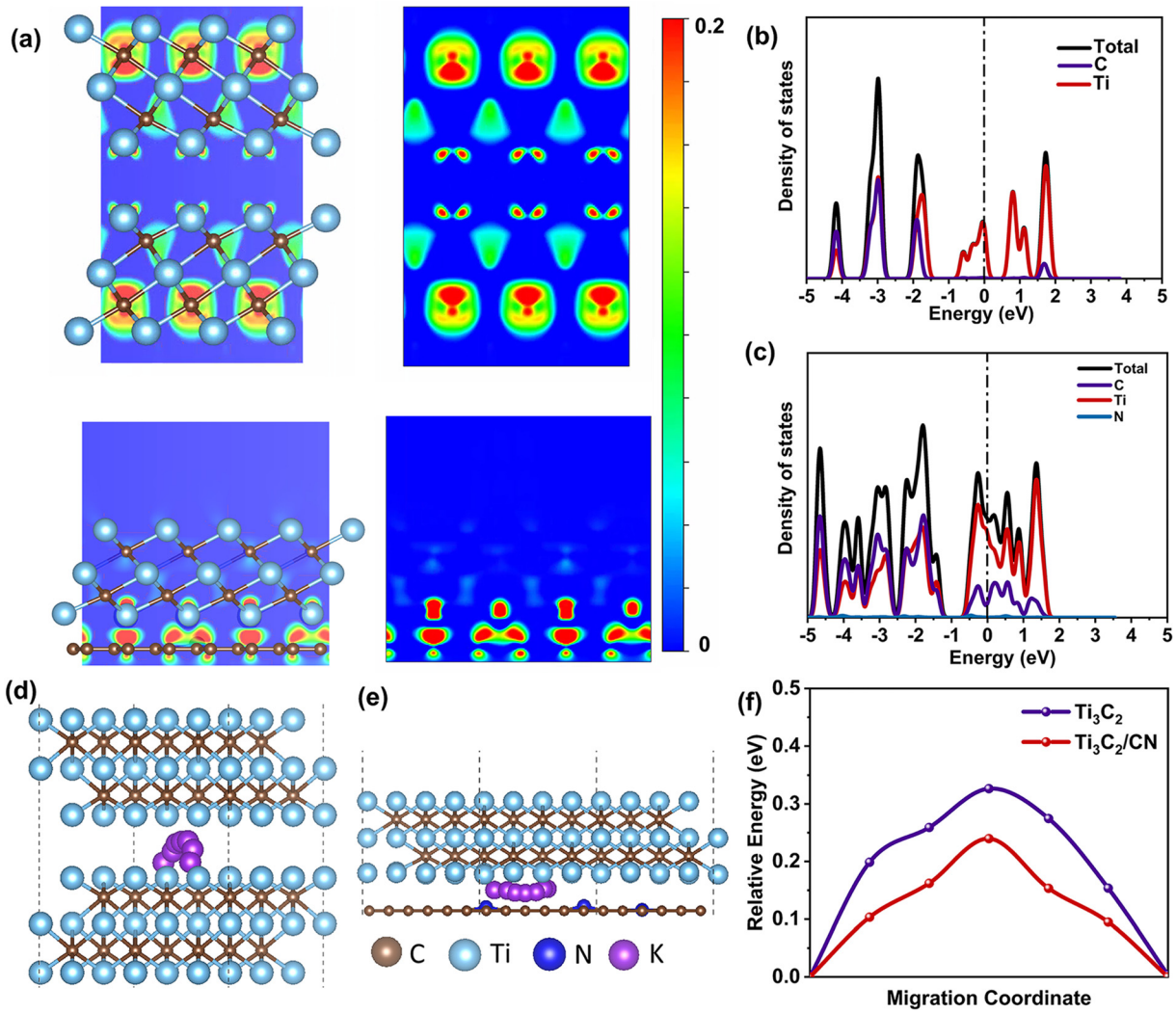

Fig. 6 (a) Charge density difference (CDD) of Ti_3C_2 structure and the interfacial structure between Ti_3C_2 and N-doped carbon. (b and c) Total and partial densities of states (DOSs) of Ti_3C_2 and Ti_3C_2/CN. (d and e) The migration path of K^+ in Ti_3C_2 and Ti_3C_2/CN. (f) K^+ migration coordinate of Ti_3C_2 and Ti_3C_2/CN.

transport capability, high-efficiency ion diffusion ability and rich electrochemical activity. Furthermore, the galvanostatic intermittent titration technique (GITT) was tested to confirm the results (Fig. 5g and S9–11†). We quantitatively calculated the coefficient D_K value using the following equation:

$$D_K = \frac{4}{(\pi\tau)(mV\Delta E_s)^2(MS\Delta E_\tau)^2}. \quad (3)$$

Fig. 5g shows that the ionic diffusion coefficients of the three samples are in the range of $10^{-7.8}$–$10^{-6.6}$ cm^2 s^{-1}, where the K^+ diffusion coefficient of the CoN-CNT@SMXene electrode is significantly higher than that of the Co@SMXene and SMXene electrodes. Consequently, the potassium-ion diffusion coefficient of the CoN-CNT@SMXene is better than that of others, indicating that the presence of N-doped CNT significantly improves the rapid diffusion ability of K^+ ions.

First-principles calculations were adopted to analyse the conductivity of electrons and the diffusion properties of ions in the composite system. The polyhedral model of MXene is shown in Fig. 5h. For further understanding of the conductivity of the CoN-CNT@SMXene, we constructed a nitrogen-doped carbon layer on the models of the Ti_3C_2 surface and marked it as Ti_3C_2/CN (Fig. 5i).

To describe the charge interaction between the Ti_3C_2 layer and the N-doped carbon nanotube, we also calculated the charge density difference (CDD) of the Ti_3C_2 structure and the interfacial structure between Ti_3C_2 and N-doped carbon (Ti_3C_2/CN). In Fig. 6a, compared to the pristine charge distribution of Ti_3C_2, Ti_3C_2/CN shows that the interface between Ti_3C_2 and N-doped carbon has a high charge density, indicating that N-doped carbon builds a charge transfer channel between the MXene spheres, thus improving their electrical conductivity. Fig. 6b and c shows the total density of states (TDOS) and partial DOS (PDOS) of Ti_3C_2 and Ti_3C_2/CN. As expected, the Ti_3C_2/CN exhibits stronger metallic properties owing to the increased TDOS intensities compared to the Ti_3C_2. Thus, the enhanced metallic characteristics of N-doped carbon nanotubes are conducive to ameliorating the conductivity of Ti_3C_2 (Fig. 6b and c).[62] Fig. 6d, e and Fig. S12† depict a representative optimized ion diffusion diagram of K^+ on the surface of monolayer Ti_3C_2 and Ti_3C_2/CN. It is clearly demonstrated that the K^+ migration energy barrier for Ti_3C_2/CN interface is significantly lower than that for pure Ti_3C_2 (Fig. 6f).[63] Compared with Ti_3C_2, the ion diffusion ability of Ti_3C_2/CN nanosheets is the best, indicating that ZIF-67-derived carbon nanotubes could endow the excellent rate capacity of CoN-CNT@SMXene electrodes.

4 Conclusions

In summary, we rationally designed a hollow CoN-CNT@SMXene composite, which is composed of planted nitrogen-doped carbon nanotubes with embedded cobalt on hollow MXene spheres. DFT calculations indicate that the CoN-CNT@SMXene can enhance electron conduction and reduce the potassium ion diffusion barrier. Furthermore, experimental results prove that cross-linked nanotubes significantly enhance the connection of hollow MXene spheres and provide a superior electron and ion migration bridge. Benefitting from its unique 3D structure, the CoN-CNT@SMXene electrode exhibited remarkable capacity (306 mA h g^{-1} at 100 mA g^{-1}), rate capability (231 mA h g^{-1} at 3.2 A g^{-1}) and cycling performance (253 mA h g^{-1} at 400 mA g^{-1} for 1000 cycles). This study provides a way to design high-performance MXene-based materials for energy storage applications in the future.

Author contributions

Xiaoyu Chen: methodology, formal analysis, visualization, writing – original draft. Shuanghong Xia: formal analysis, visualization. Tianyu Tan: formal analysis, methodology. Yajing Zhu: methodology, formal analysis, writing – original draft. Ling Li: visualization, formal analysis, methodology. Qiancheng Zhu: formal analysis, methodology, writing – review & editing. Wenming Zhang: conceptualization, methodology, formal analysis, supervision.

Conflicts of interest

There are no conflicts to declare.

Acknowledgements

We gratefully acknowledge the financial support from the following sources: National Natural Science Foundation of China (NSFC) (Grants 52171206, 51762013), Subtask of National Key R&D Program of China (2016YFF0203103-3, 2017YFC0805703). Young Talent of Hebei Province (No. 70280011808, 70280016160250), Hebei Province Outstanding Youth Fund (A2018201019, A2017201082), Hebei Province Natural Science Fund (A2015201050, E2017201142).

References

1 H. Lei, J. Li, X. Zhang, L. Ma, Z. Ji, Z. Wang, L. Pan, S. Tan and W. Mai, A review of hard carbon anode: Rational design and advanced characterization in potassium ion batteries, *InfoMat*, 2022, **4**, e12272.
2 G. Luo, X. Feng, M. Qian, W. Zhang, W. Qin, C. Wu and L. Pan, State-of-art progress and perspectives on alloy-type anode materials for potassium-ion batteries, *Mater. Chem. Front.*, 2023, DOI: **10.1039/D3QM00031A**.
3 Z. Wang, W. Zhuo, J. Li, L. Ma, S. Tan, G. Zhang, H. Yin, W. Qin, H. Wang, L. Pan, A. Qin and W. Mai, Regulation of ferric iron vacancy for Prussian blue analogue cathode to realize high-performance potassium ion storage, *Nano Energy*, 2022, **98**, 107243.

4 Y. Dong, H. Shi and Z. S. Wu, Recent advances and promise of MXene-based nanostructures for high-performance metal ion batteries, *Adv. Funct. Mater.*, 2020, **30**, 2000706.
5 E. Pomerantseva, F. Bonaccorso, X. Feng, Y. Cui and Y. Gogotsi, Energy storage: the future enabled by nanomaterials, *Science*, 2019, **366**, eaan8285.
6 X. Liu, T. Ji, H. Guo, H. Wang, J. Li, H. Liu and Z. Shen, Effects of crystallinity and defects of layered carbon materials on potassium storage: a review and prediction, *Electrochem. Energy Rev.*, 2022, **5**, 401.
7 H. Qian, H. Ren, Y. Zhang, X. He, W. Li, J. Wang, J. Hu, H. Yang, H. M. K. Sari, Y. Chen and X. Li, Surface doping vs. bulk doping of cathode materials for lithium-ion batteries: a review, *Electrochem. Energy Rev.*, 2022, **5**, 2.
8 C. Yang, J. Feng, F. Lv, J. Zhou, C. Lin, K. Wang, Y. Zhang, Y. Yang, W. Wang, J. Li and S. Guo, Metallic graphene-like VSe_2 ultrathin nanosheets: superior potassium-ion storage and their working mechanism, *Adv. Mater.*, 2018, **30**, 1800036.
9 R. Zhao, H. Di, X. Hui, D. Zhao, R. Wang, C. Wang and L. Yin, Self-assembled Ti_3C_2 MXene and N-rich porous carbon hybrids as superior anodes for high-performance potassium-ion batteries, *Energy Environ. Sci.*, 2020, **13**, 246–257.
10 W. Zhang, Y. Liu and Z. Guo, Approaching high-performance potassium-ion batteries via advanced design strategies and engineering, *Sci. Adv.*, 2019, **5**, eaav7412.
11 Q. Wang, X. Zhu, Y. Liu, Y. Fang, X. Zhou and J. Bao, Rice husk-derived hard carbons as high-performance anode materials for sodium-ion batteries, *Carbon*, 2018, **127**, 658–666.
12 Y. Hao, J. Shao, Y. Yuan, X. Li, W. Xiao, H. M. K. Sari, T. Liu and J. Lu, Design of Phosphide Anodes Harvesting Superior Sodium Storage: Progress, Challenges, and Perspectives, *Adv. Funct. Mater.*, 2023, **33**, 2212692.
13 Y. Shi, P. Yin, J. Li, X. Xu, Q. Jiang, J. Li, H. M. K. Sari, J. Wang, W. Li, J. Hu, Q. Lin, J. Liu, J. Yang and X. Li, Ultrahigh rate capability of *in situ* anchoring FeF_3 cathode onto double-enhanced conductive Fe/graphitic carbon for high energy density lithium-ion batteries, *Nano Energy*, 2023, **108**, 108181.
14 H. Shan, J. Qin, J. Wang, H. M. K. Sari, L. Lei, W. Xiao, W. Li, C. Xie, H. Yang, Y. Luo, G. Zhang and X. Li, Doping-induced electronic/ionic engineering to optimize the redox kinetics for potassium storage: a case study of Ni-doped $CoSe_2$, *Adv. Sci.*, 2022, **9**, 2200341.
15 J. Liu, P. Kopold, P. A. Van aken, J. Maier and Y. Yu, Energy storage materials from nature through nanotechnology: a sustainable route from reed plants to a silicon anode for lithium–ion batteries, *Angew. Chem., Int. Ed.*, 2015, **54**, 9632–9636.
16 M. Chen, L. Wang, X. Sheng, T. Wang, J. Zhou, S. Li, X. Shen, M. Zhang, Q. Zhang, X. Yu, J. Zhu and B. Lu, An ultrastable nonaqueous potassium–ion hybrid capacitor, *Adv. Funct. Mater.*, 2020, **30**, 2004247.
17 A. K. Geim and K. S. Novoselov, The rise of graphene, *Nat. Nanotechnol.*, 2010, **5**, 755.
18 L. Wang, W. Tao, L. Yuan, Z. Liu, Q. Huang, Z. Chai, J. Gibson and W. Shi, Rational control of the interlayer space inside two-dimensional titanium carbides for highly efficient uranium removal and imprisonment, *Chem. Commun.*, 2017, **53**, 12084–12087.
19 S. Qin, D. Liu, G. Wang, D. Portehault, C. J. Garvey, Y. Gogotsi, W. Lei and Y. Chen, High and stable ionic conductivity in 2D nanofluidic ion channels between boron nitride layers, *J. Am. Chem. Soc.*, 2017, **139**, 6314–6320.
20 M. Samadi, N. Sarikhani, M. Zirak, H. Zhang, H. L. Zhang and A. Z. Moshfegh, Group 6 Transition Metal Dichalcogenide Nanomaterials: Synthesis, *Nanoscale Horiz.*, 2018, **3**, 90–204.
21 K. Leng, Z. Chen, X. Zhao, W. Tang, B. Tian, C. T. Nai, W. Zhou and K. P. Loh, Phase restructuring in transition metal dichalcogenides for highly stable energy storage, *ACS Nano*, 2016, **10**, 9208–9215.
22 J. R. Brent, N. Savjani, E. A. Lewis, S. J. Haigh, D. J. Lewis and P. Brien, Production of few-layer phosphorene by liquid exfoliation of black phosphorus, *Chem. Commun.*, 2014, **50**, 13338–13341.
23 M. Naguib, M. Kurtoglu, V. Presser, J. Lu, J. Niu, M. Heon, L. Hultman, Y. Gogotsi and M. W. Barsoum, Two–dimensional nanocrystals produced by exfoliation of Ti_3AlC_2, *Adv. Mater.*, 2011, **23**, 4248–4253.
24 D. Xiong, X. Li, Z. Bai and S. Lu, Recent advances in layered $Ti_3C_2T_x$ MXene for electrochemical energy storage, *Small*, 2018, **14**, 1703419.
25 J. Zhao, H. Liu, Z. Yu, R. Quhe, S. Zhou, Y. Wang, C. C. Liu, H. Zhong, N. Han, J. Lu, Y. Yao and K. Wu, Rise of silicene: A competitive 2D material, *Prog. Mater. Sci.*, 2016, **83**, 124–151.
26 Z. Du, S. Yang, S. Li, J. Lou, S. Zhang, S. Wang, B. Li, Y. Gong, S. Li, X. Zou and P. M. Ajayan, Conversion of non-van der Waals solids to 2D transition-metal chalcogenides, *Nature*, 2020, **577**, 492–496.
27 K. R. Babu, N. Zhu and H. Bao, Iron-Catalyzed C–H Alkylation of Heterocyclic C–H Bonds, *Org. Lett.*, 2017, **19**, 46–49.
28 M. Naguib, O. Mashtalir, J. Carle, V. Presser, J. Lu, L. Hultman, Y. Gogotsi and M. W. Barsoum, Two-dimensional transition metal carbides, *ACS Nano*, 2012, **6**, 1322–1331.
29 B. Anasori, Y. Xie, M. Beidaghi, J. Lu, B. C. Hosler, L. Hultman, P. Kent, Y. Gogotsi and M. W. Barsoum, Two-dimensional, ordered, double transition metals carbides (MXenes, *ACS Nano*, 2015, **9**, 9507–9516.
30 M. Alhabeb, K. Maleski, T. S. Mathis, A. Sarycheva, C. B. Hatter, S. Uzun, A. Levitt and Y. Gogotsi, Selective etching of silicon from Ti_3SiC_2 (MAX) to obtain 2D titanium carbide (MXene), *Angew. Chem., Int. Ed.*, 2018, **57**, 5444–5448.
31 Z. Yuan, L. Wang, D. Li, J. Cao and W. Han, Carbon-reinforced Nb_2CT_x MXene/MoS_2 nanosheets as a superior

rate and high-capacity anode for sodium-ion batteries, *ACS Nano*, 2021, **15**, 7439–7450.

32 G. Deysher, C. E. Shuck, K. Hantanasirisakul, N. C. Frey, A. C. Foucher, K. Maleski, A. Sarycheva, V. B. Shenoy, A. Stach, B. Anasori and Y. Gogotsi, Synthesis of Mo_4VAlC_4 MAX phase and two-dimensional Mo_4VC_4 MXene with five atomic layers of transition metals, *ACS Nano*, 2019, **14**, 204–217.

33 M. Q. Zhao, X. Xie, C. E. Ren, T. Makaryan, B. Anasori, G. Wang and Y. Gogotsi, Hollow MXene spheres and 3D macroporous MXene frameworks for Na–ion storage, *Adv. Mater.*, 2017, **29**, 1702410.

34 M. Han, K. Maleski, C. E. Shuck, Y. Yang, J. T. Glazar, A. C. Foucher, K. Hantanasirisakul, A. Sarycheva, N. C. Frey, S. J. May, V. B. Shenoy, E. A. Stach and Y. Gogotsi, Tailoring electronic and optical properties of MXenes through forming solid solutions, *J. Am. Chem. Soc.*, 2020, **142**, 19110–19118.

35 P. Srivastava, A. Mishra, H. Mizuseki, K.-R. Lee and A. Singh, Mechanistic insight into the chemical exfoliation and functionalization of Ti_3C_2 MXene, *ACS Appl. Mater. Interfaces*, 2016, **8**, 24256–24264.

36 M. Naguib, V. N. Mochalin, M. W. Barsoum and Y. Gogotsi, 25th Anniversary Article: MXenes: A New Family of Two–Dimensional Materials, *Adv. Mater.*, 2014, **26**, 992–1005.

37 M. R. Lukatskaya, S. Kota, Z. Lin, M.-Q. Zhao, N. Shpigel, M. D. Levi, J. Hallim, P.-L. Taberna, M. W. Barsoum, P. Simon and Y. Goaotsi, Ultra-high-rate pseudocapacitive energy storage in two-dimensional transition metal carbides, *Nat. Energy*, 2017, **2**, 17105.

38 D. Pinto, B. Anasori, H. Avireddy, C. E. Shuck, K. Hantanasirisakul, G. Deysher, J. R. Morante, W. Porzio, H. N. Alshareef and Y. Gogotsi, Synthesis and electrochemical properties of 2D molybdenum vanadium carbides–solid solution MXenes, *J. Mater. Chem. A*, 2020, **8**, 8957–8968.

39 Y. Wang, X. Wang, X. Li, Y. Bai, H. Xiao, Y. Liu, R. Liu and G. Yuan, Engineering 3D ion transport channels for flexible MXene films with superior capacitive performance, *Adv. Funct. Mater.*, 2019, **29**, 1900326.

40 M. Boota, B. Anasori, C. Voigt, M.-Q. Zhao, M. W. Barsoum and Y. Gogotsi, Pseudocapacitive electrodes produced by oxidant–free polymerization of pyrrole between the layers of 2D titanium carbide (MXene), *Adv. Mater.*, 2016, **28**, 1517–1522.

41 L. Ding, Y. Wei, Y. Wang, H. Chen, J. Caro and H. Wang, A two–dimensional lamellar membrane: MXene nanosheet stacks, *Angew. Chem., Int. Ed.*, 2017, **56**, 1825–1829.

42 Z. Ling, C. E. Ren, M.-Q. Zhao and Y. Gogotsi, Flexible and conductive MXene films and nanocomposites with high capacitance, *Proc. Natl. Acad. Sci. U. S. A.*, 2014, **111**, 16676–16681.

43 J. Zhou, J. Yu, L. Shi, Z. Wang, H. Liu, B. Yang, C. Li, C. Zhu and J. Xu, A conductive and highly deformable all–pseudocapacitive composite paper as supercapacitor electrode with improved areal and volumetric capacitance, *Small*, 2018, **14**, 1803786.

44 Q. Zhao, Q. Zhu, J. Miao, P. Zhang, L. He and B. Xu, Flexible 3D porous MXene foam for high–performance lithium–ion batteries, *Small*, 2019, **15**, 1904293.

45 Y. Xia, T. S. Mathis, M.-Q. Zhao, B. Anasori, A. Dang, Z. Zhou, H. Cho, Y. Gogotsi and S. Yang, Thickness-independent capacitance of vertically aligned liquid-crystalline MXenes, *Nature*, 2018, **557**, 409–412.

46 G. Kresse and J. Furthmüller, Efficient Iterative Schemes for Ab Initio Total-Energy Calculations Using a Plane-Wave Basis Set, *Phys. Rev. B: Condens. Matter Mater. Phys.*, 1996, **54**, 11169–11186.

47 J. P. Perdew, K. Burke and M. Ernzerhof, Generalized Gradient Approximation Made Simple, *Phys. Rev. Lett.*, 1997, **78**, 3865–3868.

48 G. Kresse and D. Joubert, From Ultrasoft Pseudopotentials to the Projector Augmented-Wave Method, *Phys. Rev. B: Condens. Matter Mater. Phys.*, 1999, **60**, 1758–1775.

49 P. E. Blöchl, Projector Augmented-Wave Method, *Phys. Rev. B: Condens. Matter Mater. Phys.*, 1994, **50**, 17953–17979.

50 S. Grimme, J. Antony, S. Ehrlich and H. Krieg, A consistent and accurate ab initio parametrization of density functional dispersion correction (DFT-D) for the 94 elements H-Pu, *J. Chem. Phys.*, 2010, **132**, 154104.

51 G. Henkelman, B. P. Uberuaga and H. Jonsson, A climbing image nudged elastic band method for finding saddle points and minimum energy paths, *J. Chem. Phys.*, 2000, **113**, 9901.

52 S. Niu, Z. Wang, M. Yu, M. Yu, L. Xiu, S. Wang, X. Wu and J. Qiu, MXene-based electrode with enhanced pseudocapacitance and volumetric capacity for power-type and ultra-long life lithium storage, *ACS nano*, 2018, **12**, 3928–3937.

53 C. Xiong, G. Zhu, H. Jiang, Q. Chen and T. Zhao, Achieving multiplexed functionality in a hierarchical MXene-based sulfur host for high-rate, high-loading lithium-sulfur batteries, *Energy Storage Mater.*, 2020, **33**, 147–157.

54 L. Li, M. Zhang, X. Zhang and Z. Zhang, New Ti_3C_2 aerogel as promising negative electrode materials for asymmetric supercapacitors, *J. Power Sources*, 2017, **364**, 234–241.

55 L.-C. Yin, J. Liang, G.-M. Zhou, F. Li, R. Saito and H.-M. Cheng, Understanding the interactions between lithium polysulfides and N-doped graphene using density functional theory calculations, *Nano Energy*, 2016, **25**, 203–210.

56 J. Zhang, N. Kong, D. Hegh, K. Usman, G. Guan, S. Qin, I. Jurewicz, W. Yang and J. M. Razal, Freezing titanium carbide aqueous dispersions for ultra-long-term storage, *ACS Appl. Mater. Interfaces*, 2020, **12**, 34032–34040.

57 Y. Wu, Y. Sun, J. Zheng, J. Rong, H. Li and L. Niu, MXenes: advanced materials in potassium ion batteries, *Chem. Eng. J.*, 2020, **404**, 126565.

58 P. Lian, Y. Dong, Z. Wu, S. Zheng, X. Wang, S. Wang, C. Sun, J. Qin, X. Shi and X. Bao, Alkalized Ti_3C_2 mxene nanoribbons with expanded interlayer spacing for high-

capacity sodium and potassium ion batteries, *Nano Energy*, 2017, **40**, 1–8.

59 J. Cao, Z. Sun, J. Li, Y. Zhu, Z. Yuan, Y. Zhang, D. Li, L. Wang and W. Han, Microbe-assisted assembly of $Ti_3C_2T_x$ MXene on fungi-derived nanoribbon heterostructures for ultrastable sodium and potassium ion storage, *ACS Nano*, 2021, **15**, 3423–3433.

60 Y. Jiang and J. Liu, Definitions of pseudocapacitive materials: a brief review, *Energy Environ. Mater.*, 2019, **2**, 30–37.

61 Y. Ding, W. Wang, M. Bi, J. Guo and Z. Fang, CoTe nanorods/rGO composites as a potential anode material for sodium-ion storage, *Electrochim. Acta*, 2019, **313**, 331–340.

62 Y. Dong, P. Liang, H. Zheng and H. Shu, G-Si_xC_y as an anode material for potassium-ion batteries insight from first principles, *Mater. Chem. Phys.*, 2021, **266**, 124541.

63 D. Er, J. Li, M. Naguib, Y. Gogotsi and V. B. Shenoy, Ti_3C_2 MXene as a high capacity electrode material for metal (Li, Na, K, Ca) ion batteries, *ACS Appl. Mater. Interfaces*, 2014, **6**, 11173–11179.